THE JOURNAL OF
PHYSICAL CHEMISTRY
LETTERS
A JOURNAL OF THE AMERICAN CHEMICAL SOCIETY

pubs.acs.org/JPCL Letter

Thermally Activated Optical Absorption into Polaronic States in Hematite

Jacob L. Shelton and Kathryn E. Knowles*

Cite This: *J. Phys. Chem. Lett.* 2021, 12, 3343−3351 Read Online

ACCESS | Metrics & More | Article Recommendations | Supporting Information

ABSTRACT: Polaron formation, whereby an electron or hole strongly couples to a lattice distortion, inhibits the carrier mobility of many first-row transition metal oxide semiconductors. Recently reported XUV transient absorption measurements of hematite (α-Fe_2O_3) demonstrate formation of electron small polarons upon photoexcitation into an undistorted charge-transfer state followed by subpicosecond lattice reorganization. Here, we show that polaronic states of hematite can be accessed directly via optical transitions from the ground state in a thermally activated lattice. Thermal difference spectra collected from 30 to 573 K combined with Stokes resonance Raman spectra indicate strong coupling between optical transitions near the band-edge (2.1−2.3 eV) and zone-center a_{1g} and longitudinal (LO) optical phonons. Density functional theory calculations of the electronic and vibrational structures of pristine and polaron-distorted hematite lattices confirm that the geometric distortion corresponding to electron small polaron formation lies along the 28-meV a_{1g} and 81-meV LO phonon coordinates and reproduce the features observed in the experimental thermal difference and resonance Raman spectra.

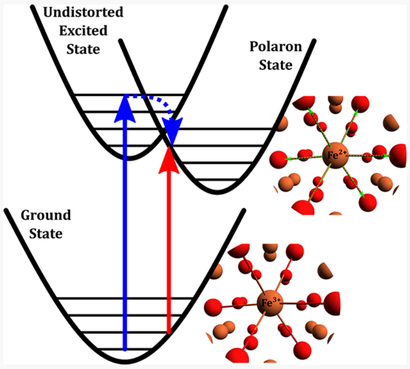

Hematite (α-Fe_2O_3) has been the subject of extensive study throughout the past decade for its potential light-harvesting applications, particularly solar-driven water oxidation, because of its narrow bandgap (2.1 eV) and favorable valence band alignment.[1−4] Unfortunately, hematite consistently displays poor photocatalytic performance as a result of the low mobility and short lifetime of its photogenerated carriers.[5−7] Both limitations have been attributed to strong carrier−phonon interactions that give rise to rapid charge trapping and nonradiative recombination pathways that dominate the decay of hematite's photoexcited state.[8−11] Characterization of these phonon-coupled optical processes is therefore critical for the rational design of efficient hematite photoanode devices.

In ground-state hematite, efficient charge transport is limited by a polaron-hopping conduction mechanism. Localized carriers, typically introduced by oxygen vacancies or dopant atoms, couple to proximal lattice distortions and form highly immobilized quasiparticles known as small polarons.[12−17] Recent visible-pump/XUV-probe transient absorption (TA) studies of undoped hematite thin films have demonstrated that small polarons also form in response to optical excitation.[18,19] In the proposed mechanism, the polaron state is populated from an intermediate photoexcited charge-transfer state following a subpicosecond reorganization of the lattice. Initially, photoexcitation at 3.1 eV excites electrons from valence band states of predominantly O 2p character to conduction bands of predominantly Fe 3d character. The resulting nonequilibrium distribution of hot electrons thermalizes rapidly (τ < 100 fs) to the conduction band-edge via emission of optical phonons, vibrationally exciting the lattice. An excited electron may then couple to an emitted phonon to form a small polaron localized to a single iron atom.[18−20]

Because charge-transfer excitations from O 2p valence bands to Fe 3d conduction bands dominate the absorption spectrum of hematite throughout the visible region,[21] the dynamic photogeneration of small polarons is also expected to impact the visible-pump/visible-probe transient absorption spectrum of hematite. Although numerous visible-pump/visible-probe transient absorption studies of hematite have been reported, they offer inconsistent interpretations of the spectral features.[22−27] Three distinct, long-lived (τ > 1 ns) positive absorption features are consistently observed to dominate the spectrum (2.0−2.7 eV) following optical excitation above the band gap. Their prevalence has inspired a variety of assignments that include excited-state absorption of both holes[22,23] and electrons[27] and often invoke the participation of midgap defect or surface states.[22−25] One of the most thorough investigations to date of hematite's visible transient absorption spectrum was performed by Hayes et al., who found that the dominant features were fully reproduced in a steady-state thermal difference spectrum (TDS), in which the ground-state

Received: December 21, 2020
Accepted: March 22, 2021
Published: March 29, 2021

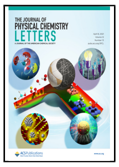

https://doi.org/10.1021/acs.jpclett.0c03751

absorption spectrum of a hematite film at room temperature is subtracted from that acquired at an elevated temperature.[28] Their results suggest that the observed transient spectrum arises almost entirely from ground-state optical transitions perturbed by thermal energy deposited into the lattice following photoexcitation.

Herein, we seek to shed new light on the optical and polaronic properties of hematite thin films by combining ground-state electronic and vibrational spectroscopies with density functional theory (DFT) electronic and vibrational structure computations. Optically induced electron small polarons in hematite have been previously proposed to form only from an intermediate photoexcited state; however, here we present evidence that the electronic states associated with the small polaron are, in fact, optically accessible directly from the ground state. We propose that this process is facilitated by optical transitions into electronic states coupled to zone-center 28-meV a_{1g} and 81-meV LO phonons that originate from (i) a thermal population governed by Bose−Einstein statistics or (ii) a coherent two-phonon scattering process indicated by the observation of resonance-enhanced second-order Raman peaks. Lattice deformations arising from these phonons, specifically the elongation of iron−oxygen bonds around a fraction of iron sites, perturb the electronic structure to create electronic states localized at these distorted iron sites. Optical transitions into these localized states produce small polarons and give rise to the ubiquitous features observed in the visible transient absorption and thermal difference spectra of hematite.

Identifying Thermally Activated Optical Transitions in Hematite. Thin films of polycrystalline hematite were prepared by a citric acid sol−gel method adapted from previous reports (see the Supporting Information for details).[29] We present a novel application of the Fresnel model derived by Barybin and Shapovalov to extract both the real and imaginary parts of the complex dielectric function of hematite from transmission and specular reflection measurements of our thin films.[30] By compiling spectra of multiple films that vary in both thickness and substrate composition, we construct a robust system of Fresnel equations and solve simultaneously for the real (n_r) and imaginary (n_i) components of the complex refractive index as well as the thickness of each film. The components of the refractive index are readily converted to those of the complex dielectric function (ϵ_r and ϵ_i) using eqs 1 and 2.

$$\epsilon_r = n_r^{\,2} - n_i^{\,2} \tag{1}$$

$$\epsilon_i = 2n_r n_i \tag{2}$$

The components of the dielectric function of hematite obtained from this procedure are shown in Figure 1a and are consistent with previously reported spectra obtained by alternative methods.[31] As illustrated in Figure 1b, the modeled dielectric function produces transmission and reflection spectra that display excellent agreement with the measured spectra. Additionally, physical measurements of film thickness by atomic force microscopy (AFM) match modeled values to within 2%. Additional figures showing the resulting fits and details of the AFM measurements are presented in Figures S1 and S2 of the Supporting Information.

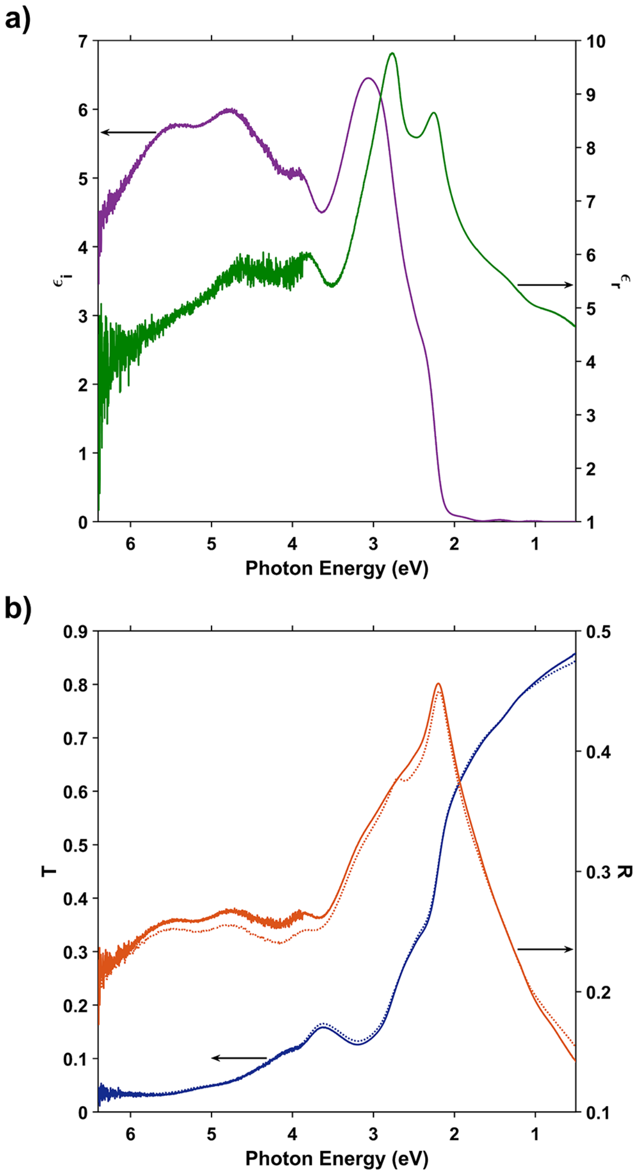

Figure 1. (a) Real (green) and imaginary (purple) components of the complex dielectric function of hematite derived from a Fresnel analysis of measured transmission and reflection spectra of three unique hematite thin films: two 3-layer films deposited on sapphire and quartz substrates and a 9-layer film deposited on sapphire. (b) Comparison of transmission (dark blue) and reflection (orange) spectra measured for a 46-nm-thick film on sapphire (solid lines) with those produced by the modeled dielectric function (dotted lines).

Thermal difference spectra, shown in Figure 2a,b, illustrate the temperature dependence of the imaginary dielectric function of hematite. Above room temperature ($T > 294$ K), three positive features corresponding to increased absorption appear in the visible region of the spectrum (2.0−2.7 eV) along with a bleach at 3.1 eV. The same features appear in the spectra collected below room temperature ($T < 294$ K) but with opposite sign. Importantly, the entire thermal difference spectrum exhibits minimal changes in intensity for $T < 80$ K. The features are the result of a convolution of thermal broadening of electronic states, shifts in band positions induced by thermal expansion of the lattice, and the growth of phonon-coupled transitions with increasing temperature.[32,33] Corresponding differential spectra of the real component of the dielectric function can be found in Figure S3 of the Supporting Information.

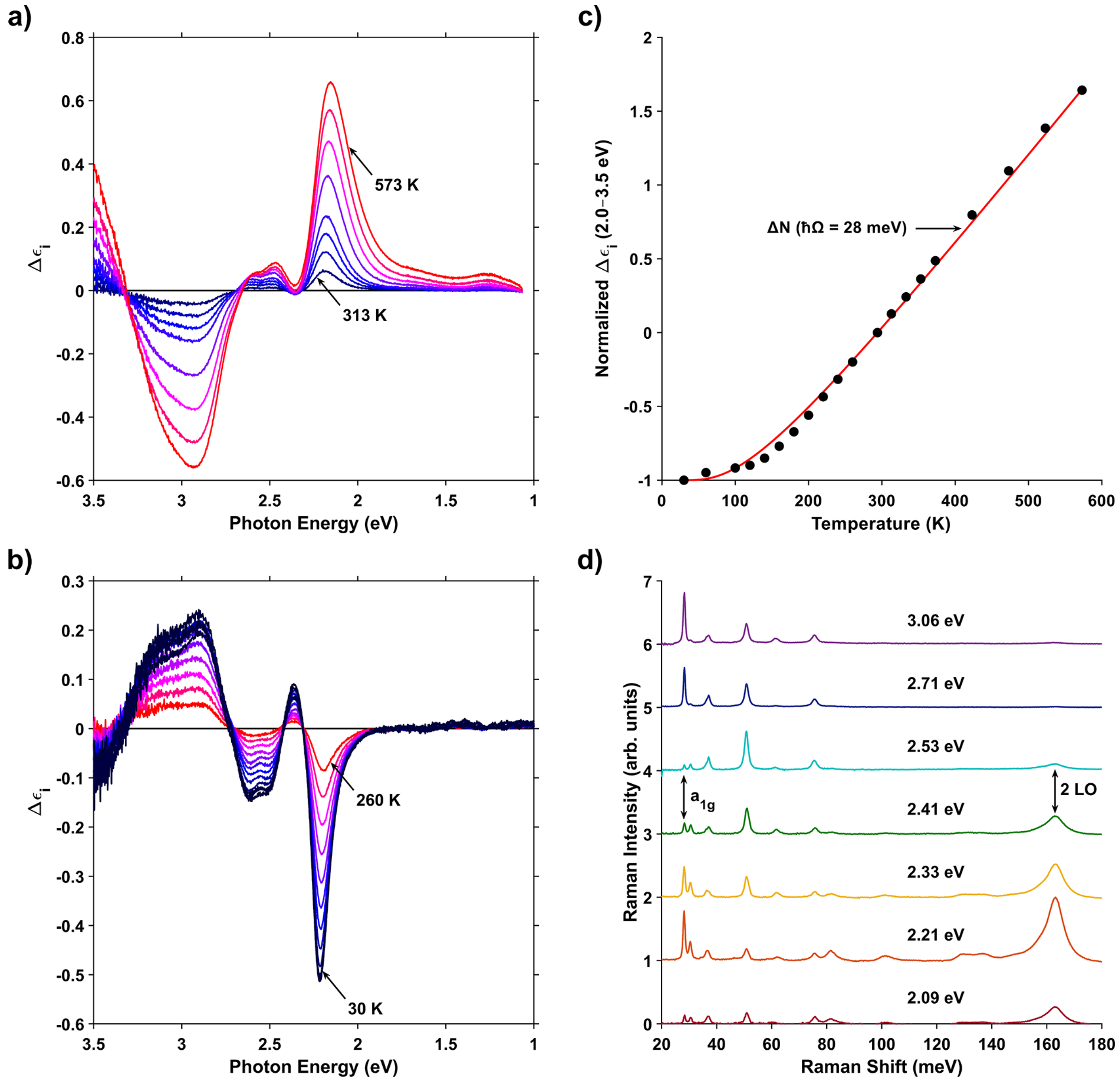

Figure 2. (a and b) Thermal difference spectra of the imaginary dielectric function of a 55-nm-thick hematite film on quartz collected at high (a) and low (b) temperatures. Spectra are plotted relative to the room temperature (294 K) imaginary dielectric function. (c) The temperature dependence of the intensity of the thermal difference spectra integrated over the interval 2.0−3.5 eV (black circles) matches the expected change in the population number (ΔN) of a 28-meV phonon (red line) calculated from eq 3. Both functions are normalized to their values at T = 30 K. (d) Stokes resonance Raman spectra of a 46-nm-thick hematite film on sapphire at various excitation photon energies. The 28-meV a_{1g} optical phonon and the 163-meV 2 LO band are indicated by arrows. Spectra are offset for clarity.

The intensities of thermally activated optical transitions depend on the population number(s) (N) of the involved phonon(s). The population of a phonon mode of energy $\hbar\Omega$ is given by the product of its density of states, $\rho(\hbar\Omega)$, and the Bose−Einstein distribution and increases with temperature as defined by eq 3 where k is the Boltzmann constant.

$$N = (e^{\hbar\Omega/kT} - 1)^{-1} \times \rho(\hbar\Omega) \tag{3}$$

Therefore, we consider the magnitude of $\Delta\epsilon_i$ to be directly proportional to the change in population number (ΔN) of the participating phonons. Normalization of the differential spectra to an arbitrary temperature, in this case 30 K, leads to eq 4.

$$\frac{\Delta\epsilon_i(\hbar\omega, T)}{|\Delta\epsilon_i(\hbar\omega, 30\ \mathrm{K})|} = \frac{\Delta N(T)}{|\Delta N(30\ \mathrm{K})|} \tag{4}$$

Figure 2c plots the total intensity of the thermal difference spectrum integrated over the interval 2.0−3.5 eV versus temperature. To account for the changes in sign that occur in this interval, we define the total intensity to be the negative absolute value for spectra collected at temperatures below 294 K and the positive absolute value for spectra collected at temperatures above 294 K. The temperature dependence of this integrated intensity overlays well with the change in population number of hematite's lowest-energy Raman-active optical phonon ($\hbar\Omega$ = 28 meV).[34] These data indicate that optical transitions in the visible region of the spectrum are coupled strongly to a thermal population of 28-meV a_{1g} phonons.

To further characterize the specific phonon modes responsible for the optical transitions observed in the thermal difference spectrum, we utilize Stokes resonance Raman

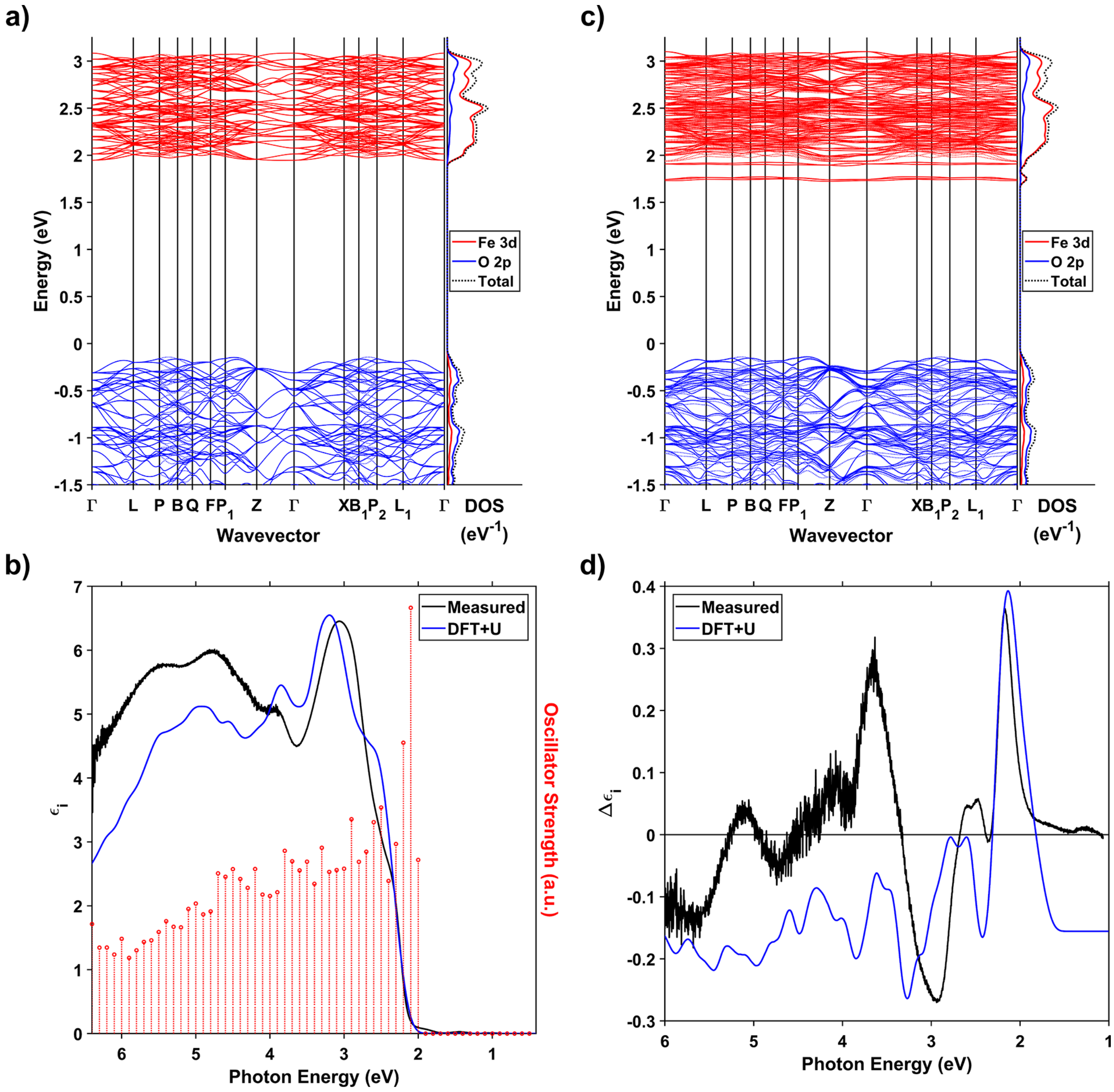

Figure 3. (a) Electronic band dispersion of a 2×2×2 supercell of pristine rhombohedral hematite. Spin-up (solid lines) and spin-down (dotted lines) bands are degenerate throughout the majority of the Brillouin zone and have identical contributions to the total density of states. Zero energy corresponds to the highest occupied state. (b) The calculated imaginary dielectric function of pristine hematite (blue line) displays excellent agreement with the measured spectrum (black line). Average oscillator strengths (red circles) are derived from momentum matrix elements coupling each pair of valence and conduction bands. (c) Small-polaron distortion breaks the spin symmetry of the hematite lattice and gives rise to five weakly dispersive bands in the spin-up channel localized to a single iron center. (d) The difference between the calculated imaginary dielectric functions of polaron-distorted and pristine hematite structures yields a differential spectrum (blue) that reproduces the features of the thermal difference spectrum collected at 373 K (black). The calculated spectrum is scaled for comparison.

spectroscopy. Raman spectra of a 46 nm thick hematite film on sapphire collected at various excitation photon energies are shown in Figure 2d. First-order peaks observed between 20 and 90 meV are characteristic of hematite.[34] Relative scattering intensities exhibit a strong dependence on excitation energy. Most notably, the band at 28 meV is significantly enhanced in the 2.2−2.3 eV excitation region, the same region in which the most intense feature of the thermal difference spectrum appears. The band is similarly enhanced under 2.7−3.1 eV excitation; however, this is due primarily to the larger extinction coefficient in that region. As demonstrated in Figure S4 of the Supporting Information, when the resonance Raman excitation profile of the 28-meV phonon mode is normalized to the value of the extinction coefficient, the resonance enhancement of the 28-meV mode is seven times larger when excited at 2.2 eV than when excited at 3.1 eV, despite the fact that the extinction coefficient is 2 orders of magnitude larger at 3.1 eV than at 2.2 eV. The 28-meV phonon is identified as a doubly degenerate a_{1g} stretching mode and the lowest-energy Raman-active optical phonon in hematite.[34] Selective enhancement at 2.1−2.2 eV excitation occurs throughout the entire Raman spectrum but is particularly pronounced for features with Raman shifts of 81 and 163 meV. The 81-meV peak is assigned to a longitudinal optical (LO) phonon.[34] The origin of the broad feature at 163 meV has not been assigned definitively, but it is most commonly attributed

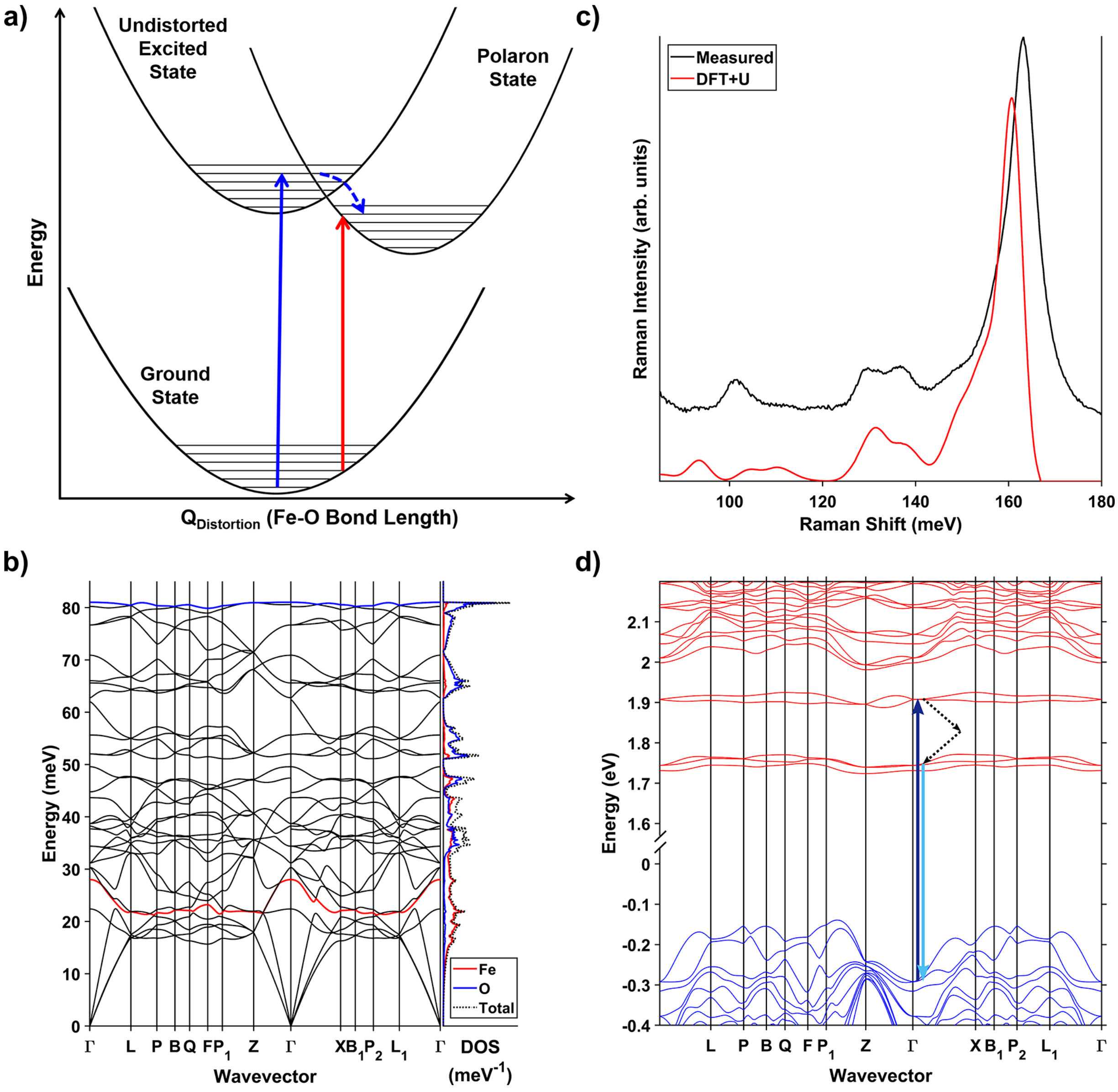

Figure 4. (a) Conceptual configuration coordinate diagram illustrating direct excitation of a polaron state from a thermally activated ground state (blue arrow). The red arrows depict previously proposed mechanisms that require optical excitation into an intermediate undistorted charge-transfer state from which the polaron state is populated following subpicosecond lattice reorganization. (b) Phonon dispersion curves computed from a single primitive cell of pristine rhombohedral hematite. The lowest-energy a_{1g} optical phonon band is highlighted in red, while the nearly dispersionless 81 meV LO phonon band is highlighted in blue. (c) Comparison of the Stokes second-order resonance Raman spectrum measured for a 46 nm thick film on sapphire at an excitation photon energy of 2.21 eV (black) with that calculated by applying the Kramers−Heisenberg formula to the electronic and phonon dispersion curves computed using the DFT+U method (red). (d) Illustration of the two-phonon scattering process that gives rise to the intense 163 meV feature of the resonance Raman spectrum. Each black dashed arrow represents an 81 meV phonon of arbitrary wavevector. The vertical lines represent the incoming (dark blue) and scattered (light blue) photon.

to the simultaneous scattering of two 81-meV LO phonons.[35,36] Because this LO mode is Raman-inactive in a pristine hematite lattice, previous reports propose that it arises from unspecified lattice "disorder";[37] however, this assignment does not account for the significant resonance enhancement of the 163 meV feature under near band-edge excitation (2.1−2.3 eV) observed here. Raman band positions and relative intensities were found to be independent of film thickness (see Figure S5 of the Supporting Information). DFT calculations presented in the following section suggest that the 163-meV feature arises from a double-resonance enhancement of second-order (2 LO) phonon scattering processes facilitated by a polaronic optical transition.

Computational Modeling of Polaronic States in Hematite. Accurate optical characterization of an extended solid-state system requires a band-theory approach to its electronic structure. Implementation of periodic boundary conditions into DFT computations is the most direct method of investigating the complex band structure of solid-state materials. Strong electron correlation and exchange effects long precluded an accurate treatment of many first-row transition metal oxides by DFT without the use of computationally taxing hybrid functionals or many-body perturbation methods.[38,39]

This problem is now routinely mitigated with the inclusion of a Hubbard parameter (DFT+U) that accounts for the strong on-site Coulombic repulsion of *d*-electrons localized to transition metal centers without a significant increase in computational cost.[40,41] Within this framework, we model the electronic and vibrational structure and complex dielectric function of both pristine and polaron-distorted geometries of hematite.

An electronic band dispersion diagram of a pristine 2×2×2 supercell of rhombohedral hematite is shown in Figure 3a. In agreement with previous studies, the highest-energy valence bands are primarily of O 2p character while Fe 3d orbitals give rise to weakly dispersive conduction bands.[21] Within the calculated electronic structure, the lowest-energy direct and indirect gaps appear within 10 meV of one another, at 2.10 and 2.09 eV, respectively. As such, the character of the fundamental gap cannot be assigned accurately. This ambiguity has plagued both theoretical[21,42] and experimental[43−45] reports on the nature of hematite's bandgap and is due primarily to the flat, dispersionless nature of the Fe 3d conduction bands.

Figure 3b compares the calculated imaginary dielectric function of pristine ground-state hematite with the experimentally measured spectrum of a thin film at room temperature. Typically, for the calculation of solid-state optical spectra, DFT is either reinforced with hybrid functionals or abandoned completely in favor of many-body perturbation theory (MBPT) and the Bethe−Salpeter equation (BSE).[42,46] Here we demonstrate that the experimental dielectric spectrum of hematite can be accurately reproduced within the confines of an independent particle approach utilizing the standard PBE-GGA functional with a Hubbard correction. The modeled spectrum is calculated using eq 5, where V is the volume of the supercell; N_k is the total number of k-points included in the calculation; $\hat{\mathbf{p}}$ is the momentum operator; and i and f denote the initial and final states, respectively.[47]

$$\epsilon_i(\hbar\omega) = \frac{4\pi}{VN_k}\sum_{i\neq f}\sum_{k}\frac{|\langle f|\hat{\mathbf{p}}|i\rangle|^2}{(E_{f,k} - E_{i,k})^2}\delta(E_{f,k} - E_{i,k} - \hbar\omega) \tag{5}$$

Compared to the experimental spectrum, the modeled dielectric function suffers primarily from an overestimation of the intensity at the band-edge and a slight displacement in the energetic positions of some features. We note that any contribution from excitonic effects to the optical response are neglected here, as excitons inherently arise from many-body interactions that can be treated only with a higher level of theory (MBPT/BSE).

Upon relaxation of the lattice geometry, an additional negative charge introduced into the hematite supercell localizes to a single iron center instead of delocalizing across the lattice in a conduction band state. The Fe−O bond lengths around the effectively reduced iron atom are elongated by 0.06 Å, equivalent to a 3% expansion. The resulting distortion is confined to the dimensions of a single primitive cell indicating the formation of an electron small polaron. Figure 3c shows the electronic structure of a neutral supercell of hematite containing the polaronic lattice distortion. Expansion of the Fe−O bonds around a single iron center shifts five spin-up conduction bands to energies just below the conduction band-edge, thus breaking the spin symmetry of the lattice. These localized bands correspond to the e_g and t_{2g} levels of the iron atom at the center of the distortion. When a second charge is introduced to the polaron-distorted lattice, it localizes in the spin-down channel, nearly restoring the spin degeneracy of the system (see Figure S6 of the Supporting Information). The bipolaronic band structure is essentially identical to that of the spin-up channel of the singly distorted lattice, indicating that the 2×2×2 supercell is sufficiently large to model an isolated polaron.

Subtracting the computed imaginary dielectric function of a pristine hematite lattice from that of the polaron-distorted lattice produces a differential spectrum remarkably similar to the thermal difference spectrum, as shown in Figure 3d. The shared features suggest that the thermally activated transitions assigned to the thermal difference spectrum correspond to the same geometric perturbations associated with small polaron formation.

In order to model the second-order Raman scattering process, we computed the phonon dispersion curve for a single primitive cell of pristine rhombohedral hematite shown in Figure 4b. The projected vibrational density of states indicates that the lower-energy modes (<30 meV) correspond primarily to Fe displacements, while the higher-energy modes (>50 meV) correspond primarily to O displacements. The highest-energy phonon occurs at 81 meV, which supports the assignment of features that appear at energies >81 meV in the resonance Raman spectra to second-order scattering processes. The remarkably flat dispersion of the 81-meV phonon gives rise to a very high density of vibrational states at this energy. Unlike first-order scattering, which only samples the center of the Brillouin zone, second-order processes can access the entire phonon density of states while still conserving total wavevector. Consequently, the conditions for double resonance enhancement of the 2 LO scattering process can be met at any arbitrary value of wavevector, which further explains the overwhelming intensity of the 163-meV Raman feature under band-edge excitation. Utilizing both the electronic dispersion curve of the polaron-distorted lattice and the vibrational dispersion curve of bulk hematite, an approximate second-order scattering spectrum can be calculated according to the Kramers−Heisenberg formula.[48] In this approximation, we neglect the electron−phonon coupling matrix elements and consider only momentum matrix elements that couple real electronic states. As shown in Figure 4c, the calculated spectrum reproduces all of the features of the second-order resonance Raman spectrum measured at 2.21 eV with accurate relative intensity and only minor errors in energetic position. An illustration of the scattering mechanism is shown in Figure 4d.

The vibrational structure of hematite computed here also indicates that the displacement of iron atoms immediately adjacent to the polaronic iron center and the elongation of the Fe−O bonds within the polaron occur along the same coordinates as the a_{1g} and LO phonon modes discussed previously. An illustration of both the polaronic distortion and the a_{1g} and LO displacement vectors is shown in Figure S7 of the Supporting Information. We therefore propose that the geometric distortion associated with electron small polarons in hematite arises from semilocal lattice distortions induced by LO ($\hbar\Omega$ = 81 meV) and a_{1g} ($\hbar\Omega$ = 28 meV) optical phonons. The temperature dependence of the integrated intensity of the TDS plotted in Figure 2c indicates that the a_{1g} phonons contributing to this polaronic distortion are generated by random thermal fluctuations of the lattice with a probability governed by its Bose−Einstein statistical population (eq 3). There are two possible mechanisms for the origin of the LO phonons that contribute to the polaronic distortion. The first mechanism is identical to the mechanism we propose for the origin of the a_{1g} phonons, namely, thermal fluctuations governed by Bose−Einstein statistics. According to eq 3, the extremely high density of phonon states at 81 meV results in a nonzero population of 81-meV LO phonons across the temperature range used to collect our thermal difference spectra (30−573 K); however, because $\hbar\Omega_{LO} \gg kT$, changes in the population of 81-meV LO phonons make a negligibly small contribution to the temperature dependence of the integrated intensity of the TDS plotted in Figure 2c compared to the contribution of the 28-meV phonons. Alternatively, generation of the 81-meV LO phonons that contribute to the polaronic distortion may occur simultaneously with photoexcitation via the coherent two-phonon scattering process that gives rise to the second-order Raman feature observed at 163 meV. Distinguishing precisely between these two mechanisms is beyond the scope of this study. Importantly, both mechanisms enable optical excitation of an electron from a valence band into a polaronic band to proceed in a single event via coupling to phonon-induced lattice distortions. This process, along with the dynamic mechanism proposed in previous studies, is illustrated conceptually in Figure 4a using a qualitative configurational coordinate diagram.

Direct excitation into a polaronic excited state accounts for the appearance of the Raman-inactive 81-meV LO phonon in the first-order spectrum. The loss of long-range translational symmetry in the vicinity of the polaronic distortion relaxes Raman selection rules and allows for the observation of otherwise silent modes. Interestingly, the excitation profile of the 81-meV band overlays remarkably well with the measured thermal difference spectrum (see Figure S8 of the Supporting Information), suggesting that the mode is activated exclusively by the same polaronic transitions that give rise to the band-edge features of the TDS. Furthermore, these transitions also account for the anomalously large resonance enhancement of the second-order Raman scattering peak at 163 meV under band-edge excitation. Coincidentally, the e_g−t_{2g} splitting of the polaronic bands is approximately 160 meV at nearly all wavevector values, suggesting that photoexcitation into these states could lead to double-resonance enhancement of the 2 LO scattering process that produces the 163-meV Raman feature.

In conclusion, the computational and experimental data presented here indicate that optical absorption near the bandgap of hematite directly populates polaronic states and is correlated to thermal fluctuations in the populations of the 28-meV a_{1g} and 81-meV LO phonons. The temperature dependence of the imaginary component of the dielectric function near the band-edge follows the Bose−Einstein distribution of a phonon with $\hbar\Omega$ = 28 meV, and resonance Raman measurements show significant enhancement of the same phonon under band-edge excitation. DFT calculations support this conclusion by demonstrating that the polaronic lattice distortion occurs along the a_{1g} and LO coordinates and yields the same changes in the complex dielectric function as those observed in the thermal difference spectra. Last, the calculated electronic and vibrational band structures demonstrate that hematite's long-debated[34,37] second-order resonance Raman spectrum arises from double-resonance enhancement in the vicinity of polaronic optical transitions coupled to 81-meV LO phonons. We conclude that the photoexcitation of hematite near the band-edge directly forms electron small polarons. The direct optical transition into a polaronic state proposed here does not conflict with previous reports indicating that polaron formation occurs following photoexcitation of an intermediate, undistorted charge-transfer state,[18,19] but rather it indicates a potential competing pathway. These results imply that formation of electron small polarons upon photoexcitation across the band gap of hematite is inevitable, which has significant implications for the use of hematite in light-harvesting applications. Finally, we suspect that direct optical excitation of polaron states may also occur in other first-row transition metal oxides possessing minimally dispersive bands derived from 3d orbitals along with strong carrier−phonon coupling.[49]

■ ASSOCIATED CONTENT

Supporting Information

The Supporting Information is available free of charge at https://pubs.acs.org/doi/10.1021/acs.jpclett.0c03751.

> Details of sample preparation and DFT calculations, additional optical functions and modeled spectra derived from thin-film Fresnel analysis, details of AFM film thickness measurements, real components of thermal difference spectra, resonance Raman excitation profiles of select Raman bands, an additional bipolaronic band structure, illustrations of phonon and polaron displacement vectors, and thickness-dependent resonance Raman spectra (PDF)

■ AUTHOR INFORMATION

Corresponding Author

Kathryn E. Knowles − *Department of Chemistry, University of Rochester, Rochester, New York 14627, United States;* orcid.org/0000-0001-6315-6473; Email: kknowles@ur.rochester.edu

Author

Jacob L. Shelton − *Department of Chemistry, University of Rochester, Rochester, New York 14627, United States;* orcid.org/0000-0002-7802-5545

Complete contact information is available at: https://pubs.acs.org/10.1021/acs.jpclett.0c03751

Notes

The authors declare no competing financial interest.

■ ACKNOWLEDGMENTS

The authors gratefully acknowledge financial support from the National Science Foundation (CHE 20-44462), the Valerie and Frank Furth Fund, and the University of Rochester. Raman measurements were performed at the University of Rochester Multiwavelength Raman Spectroscopy Facility funded by the National Science Foundation (CHE 14-27882), and computing support was provided by the University of Rochester Center for Integrated Research Computing. J.L.S. acknowledges Melissa D. Koch for conducting AFM measurements.

■ REFERENCES

(1) Tamirat, A. G.; Rick, J.; Dubale, A. A.; Su, W.-N.; Hwang, B.-J. Using Hematite for Photoelectrochemical Water Splitting: a Review of Current Progress and Challenges. *Nanoscale Horiz* **2016**, *1*, 243−267.

(2) Dias, P.; Vilanova, A.; Lopes, T.; Andrade, L.; Mendes, A. Extremely Stable Bare Hematite Photoanode for Solar Water Splitting. *Nano Energy* **2016**, *23*, 70−79.

(3) Shen, S.; Lindley, S. A.; Chen, X.; Zhang, J. Z. Hematite Heterostructures for Photoelectrochemical Water Splitting: Rational Materials Design and Charge Carrier Dynamics. *Energy Environ. Sci.* **2016**, *9*, 2744−2775.

(4) Iandolo, B.; Wickman, B.; Zorić, I.; Hellman, A. The Rise of Hematite: Origin and Strategies to Reduce the High Onset Potential for the Oxygen Evolution Reaction. *J. Mater. Chem. A* **2015**, *3*, 16896−16912.

(5) Liao, P.; Toroker, M. C.; Carter, E. A. Electron Transport in Pure and Doped Hematite. *Nano Lett.* **2011**, *11*, 1775−1781.

(6) Liao, P.; Carter, E. A. Hole Transport in Pure and Doped Hematite. *J. Appl. Phys.* **2012**, *112*, 013701.

(7) Herrmann-Geppert, I.; Bogdanoff, P.; Radnik, J.; Fengler, S.; Dittrich, T.; Fiechter, S. Surface Sspects of Sol−Gel Derived Hematite Films for the Photoelectrochemical Oxidation of Water. *Phys. Chem. Chem. Phys.* **2013**, *15*, 1389−1398.

(8) Sivula, K.; Le Formal, F.; Grätzel, M. Solar Water Splitting: Progress Using Hematite (α-Fe_2O_3) Photoelectrodes. *ChemSusChem* **2011**, *4*, 432−449.

(9) Pendlebury, S. R.; Wang, X.; Le Formal, F.; Cornuz, M.; Kafizas, A.; Tilley, S. D.; Grätzel, M.; Durrant, J. R. Ultrafast Charge Carrier Recombination and Trapping in Hematite Photoanodes Under Applied Bias. *J. Am. Chem. Soc.* **2014**, *136*, 9854−7.

(10) Zhou, Z.; Liu, J.; Long, R.; Li, L.; Guo, L.; Prezhdo, O. V. Control of Charge Carriers Trapping and Relaxation in Hematite by Oxygen Vacancy Charge: Ab Initio Non-adiabatic Molecular Dynamics. *J. Am. Chem. Soc.* **2017**, *139*, 6707−6717.

(11) Sharma, M.; Murugavel, S.; Shukla, D. K.; De Groot, F. M. F. Reversal in the Lattice Contraction of α-Fe_2O_3 Nanoparticles. *J. Phys. Chem. C* **2018**, *122*, 9292−9301.

(12) Katz, J. E.; Zhang, X.; Attenkofer, K.; Chapman, K. W.; Frandsen, C.; Zarzycki, P.; Rosso, K. M.; Falcone, R. W.; Waychunas, G. A.; Gilbert, B. Electron Small Polarons and Their Mobility in Iron (Oxyhydr)oxide Nanoparticles. *Science* **2012**, *337*, 1200−1203.

(13) Adelstein, N.; Neaton, J. B.; Asta, M.; De Jonghe, L. C. Density Functional Theory Based Calculation of Small-Polaron Mobility in Hematite. *Phys. Rev. B: Condens. Matter Mater. Phys.* **2014**, *89*, 245115.

(14) Lany, S. Semiconducting Transition Metal Oxides. *J. Phys.: Condens. Matter* **2015**, *27*, 283203.

(15) Lohaus, C.; Steinert, C.; Brötz, J.; Klein, A.; Jaegermann, W. Systematic Investigation of the Electronic Structure of Hematite Thin Films. *Adv. Mater. Interfaces* **2017**, *4*, 1700542.

(16) Smart, T. J.; Ping, Y. Effect of Defects on the Small Polaron Formation and Transport Properties of Hematite from First-Principles Calculations. *J. Phys.: Condens. Matter* **2017**, *29*, 394006.

(17) Biswas, S.; Wallentine, S.; Bandaranayake, S.; Baker, L. R. Controlling Polaron Formation at Hematite Surfaces by Molecular Functionalization Probed by XUV Reflection-Absorption Spectroscopy. *J. Chem. Phys.* **2019**, *151*, 104701.

(18) Carneiro, L. M.; Cushing, S. K.; Liu, C.; Su, Y.; Yang, P.; Alivisatos, A. P.; Leone, S. R. Excitation-Wavelength-Dependent Small Polaron Trapping of Photoexcited Carriers in α-Fe_2O_3. *Nat. Mater.* **2017**, *16*, 819.

(19) Husek, J.; Cirri, A.; Biswas, S.; Baker, L. R. Surface Electron Dynamics in Hematite (α-Fe_2O_3): Correlation Between Ultrafast Surface Electron Trapping and Small Polaron Formation. *Chem. Sci.* **2017**, *8*, 8170−8178.

(20) Pastor, E.; Park, J.-S.; Steier, L.; Kim, S.; Grätzel, M.; Durrant, J. R.; Walsh, A.; Bakulin, A. A. In Situ Observation of Picosecond Polaron Self-Localisation in α-Fe_2O_3 Photoelectrochemical Cells. *Nat. Commun.* **2019**, *10*, 3962.

(21) Pozun, Z. D.; Henkelman, G. Hybrid Density Functional Theory Band Structure Engineering in Hematite. *J. Chem. Phys.* **2011**, *134*, 224706.

(22) Pendlebury, S. R.; Barroso, M.; Cowan, A. J.; Sivula, K.; Tang, J.; Grätzel, M.; Klug, D.; Durrant, J. R. Dynamics of Photogenerated Holes in Nanocrystalline α-Fe_2O_3 Electrodes for Water Oxidation Probed by Transient Absorption Spectroscopy. *Chem. Commun.* **2011**, *47*, 716−718.

(23) Barroso, M.; Mesa, C. A.; Pendlebury, S. R.; Cowan, A. J.; Hisatomi, T.; Sivula, K.; Grätzel, M.; Klug, D. R.; Durrant, J. R. Dynamics of Photogenerated Holes in Surface Modified α-Fe_2O_3 Photoanodes for Solar Water Splitting. *Proc. Natl. Acad. Sci. U. S. A.* **2012**, *109*, 15640−15645.

(24) Barroso, M.; Pendlebury, S. R.; Cowan, A. J.; Durrant, J. R. Charge Carrier Trapping, Recombination and Transfer in Hematite (α-Fe_2O_3) Water Splitting Photoanodes. *Chem. Sci.* **2013**, *4*, 2724−2734.

(25) Fitzmorris, B. C.; Patete, J. M.; Smith, J.; Mascorro, X.; Adams, S.; Wong, S. S.; Zhang, J. Z. Ultrafast Transient Absorption Studies of Hematite Nanoparticles: The Effect of Particle Shape on Exciton Dynamics. *ChemSusChem* **2013**, *6*, 1907−1914.

(26) Huang, Z.; Lin, Y.; Xiang, X.; Rodríguez-Córdoba, W.; McDonald, K. J.; Hagen, K. S.; Choi, K.-S.; Brunschwig, B. S.; Musaev, D. G.; Hill, C. L.; Wang, D.; Lian, T. In Situ Probe of Photocarrier Dynamics in Water-Splitting Hematite (α-Fe_2O_3) Electrodes. *Energy Environ. Sci.* **2012**, *5*, 8923−8926.

(27) Sorenson, S.; Driscoll, E.; Haghighat, S.; Dawlaty, J. M. Ultrafast Carrier Dynamics in Hematite Films: The Role of Photoexcited Electrons in the Transient Optical Response. *J. Phys. Chem. C* **2014**, *118*, 23621−23626.

(28) Hayes, D.; Hadt, R. G.; Emery, J. D.; Cordones, A. A.; Martinson, A. B. F.; Shelby, M. L.; Fransted, K. A.; Dahlberg, P. D.; Hong, J.; Zhang, X.; Kong, Q.; Schoenlein, R. W.; Chen, L. X. Electronic and Nuclear Contributions to Time-Resolved Optical and X-ray Absorption Spectra of Hematite and Insights into Photoelectrochemical Performance. *Energy Environ. Sci.* **2016**, *9*, 3754−3769.

(29) Prévot, M. S.; Guijarro, N.; Sivula, K. Enhancing the Performance of a Robust Sol-Gel-Processed p-Type Delafossite $CuFeO_2$ photocathode for solar water reduction. *ChemSusChem* **2015**, *8*, 1359−67.

(30) Barybin, A.; Shapovalov, V. Substrate Effect on the Optical Reflectance and Transmittance of Thin-Film Structures. *Int. J. Opt.* **2010**, *2010*, 137572.

(31) Chen, C. T.; Cahan, B. D. Visible and Ultraviolet Optical Properties of Single-Crystal and Polycrystalline Hematite Measured by Spectroscopic Ellipsometry. *J. Opt. Soc. Am.* **1981**, *71*, 932−934.

(32) Zheng, J. P.; Kwok, H. S. Temperature Dependence of the Optical Properties of Semiconductor Microcrystals. *J. Opt. Soc. Am. B* **1992**, *9*, 2047−2053.

(33) Chow, W. S. Theory of Phonon-Assisted Optical Absorption in Semiconductors. I. *Phys. Rev.* **1969**, *185*, 1056−1061.

(34) Marshall, C. P.; Dufresne, W. J. B.; Rufledt, C. J. Polarized Raman Spectra of Hematite and Assignment of External modes. *J. Raman Spectrosc.* **2020**, *51*, 1522−1529.

(35) Jubb, A. M.; Allen, H. C. Vibrational Spectroscopic Characterization of Hematite, Maghemite, and Magnetite Thin Films Produced by Vapor Deposition. *ACS Appl. Mater. Interfaces* **2010**, *2*, 2804−2812.

(36) Smith, J. P.; Smith, F. C.; Booksh, K. S. Spatial and Spectral Resolution of Carbonaceous Material from Hematite (α-Fe_2O_3) Using Multivariate Curve Resolution-Alternating Least Squares (MCR-ALS) with Raman Microspectroscopic Mapping: Implications for the Search for Life on Mars. *Analyst* **2017**, *142*, 3140−3156.

(37) McCarty, K. F. Inelastic Light Scattering in α-Fe_2O_3: Phonon vs Magnon Scattering. *Solid State Commun.* **1988**, *68*, 799−802.

(38) Hasnip, P. J.; Refson, K.; Probert, M. I. J.; Yates, J. R.; Clark, S. J.; Pickard, C. J. Density Functional Theory in the Solid State. *Philos. Trans. R. Soc., A* **2014**, *372*, 20130270.

(39) Meng, Y.; Liu, X.-W.; Huo, C.-F.; Guo, W.-P.; Cao, D.-B.; Peng, Q.; Dearden, A.; Gonze, X.; Yang, Y.; Wang, J.; Jiao, H.; Li, Y.; Wen,

X.-D. When Density Functional Approximations Meet Iron Oxides. *J. Chem. Theory Comput.* **2016**, *12*, 5132−5144.

(40) Tolba, S. A.; Gameel, K. M.; Ali, B. A.; Almossalami, H. A.; Allam, N. K. The DFT+U: Approaches, Accuracy, and Applications. *IntechOpen* **2018**, DOI: 10.5772/intechopen.72020.

(41) Himmetoglu, B.; Floris, A.; de Gironcoli, S.; Cococcioni, M. Hubbard-Corrected DFT Energy Functionals: The LDA+U description of correlated systems. *Int. J. Quantum Chem.* **2014**, *114*, 14−49.

(42) Piccinin, S. The Band Structure and Optical Absorption of Hematite (α-Fe_2O_3): A First-Principles GW-BSE Study. *Phys. Chem. Chem. Phys.* **2019**, *21*, 2957−2967.

(43) Zimmermann, R.; Steiner, P.; Claessen, R.; Reinert, F.; Hüfner, S.; Blaha, P.; Dufek, P. Electronic Structure of 3d-Transition-Metal Oxides: On-Site Coulomb Repulsion Versus Covalency. *J. Phys.: Condens. Matter* **1999**, *11*, 1657−1682.

(44) Mochizuki, S. Electrical Conductivity of α-Fe_2O_3. *Phys. Status Solidi A* **1977**, *41*, 591−594.

(45) Glasscock, J. A.; Barnes, P. R. F.; Plumb, I. C.; Bendavid, A.; Martin, P. J. Structural, Optical and Electrical Properties of Undoped Polycrystalline Hematite Thin Films Produced Using Filtered Arc Deposition. *Thin Solid Films* **2008**, *516*, 1716−1724.

(46) Ahmad, F.; Agusta, M. K.; Dipojono, H. K. Electronic and Optical Properties of CuO Based on DFT+U and GW Approximation. *J. Phys.: Conf. Ser.* **2016**, *739*, 012040.

(47) Fox, A. M.; Fox, D. P. A. M. *Optical Properties of Solids*; Oxford University Press, 2001.

(48) Sakurai, J. J. *Advanced Quantum Mechanics*; Addison-Wesley Publishing Company, 1967.

(49) Smart, T. J.; Pham, T. A.; Ping, Y.; Ogitsu, T. Optical Absorption Induced by Small Polaron Formation in Transition Metal Oxides: The Case of Co_3O_4. *Phys. Rev. Mater.* **2019**, *3*, 102401.